




A nanostructured Al-doped ZnO as an ultra-sensitive room-temperature ammonia gas sensor

Bantikatta Himabindu^{1,2,*} , N. S. M. P. Latha Devi^{2,*}, Pothukanuri Nagaraju³, and Bhogoju Rajini Kanth⁴

¹Department of H&S, Sreyas Institute of Engineering and Technology, Hyderabad 500068, Telangana, India

²Department of Engineering Physics, Koneru Lakshmaiah Educational Foundation, Guntur 522302, Andhra Pradesh, India

³Department of Physics, Sreenidhi University, Hyderabad 501301, Telangana, India

⁴LSMS, Department of Physical Sciences, T.K.R. College of Engineering and Technology, Hyderabad 500097, Telangana, India

Received: 7 November 2022

Accepted: 25 March 2023

Published online:
22 April 2023

© The Author(s), under exclusive licence to Springer Science+Business Media, LLC, part of Springer Nature 2023

ABSTRACT

Novel chemi-resistive gas sensors with strong detection capabilities operating at room temperature are desirable owing to their extended cycle life, high stability, and low power consumption. The current study focuses on detecting NH₃ at room temperature using lower gas concentrations. The co-precipitation technique was employed to produce pure and Al-doped ZnO nanoparticles, which were calcined at 300 °C for three hours. The effect of aluminium (Al) doping on the structural, morphological, optical, and gas-sensing abilities was investigated and reported. The presence of aluminium was confirmed by XRD, EDX, and FTIR spectroscopy. Additionally, to assess the various characteristics of Al-doped ZnO nanoparticles, scanning electron microscopy (SEM), ultraviolet-visible diffuse reflectance spectroscopy (UV-DRS), atomic force microscopy (AFM), and Brunauer–Emmett–Teller (BET) techniques were used. The crystallite size increased from 14.82 to 17.49 nm in the XRD analysis; the SEM pictures showed a flower-like morphology; and the energy gap decreased from 3.240 to 3.210 eV when Al doping was raised from 1 wt% to 4 wt%. AFM studies revealed topographical information with significant roughness in the range of 230–43 nm. BET analysis showed a mesoporous nature with surface areas varying from 25.274 to 14.755 m²/g and pore diameters ranging from 8.34 to 7.00 nm. The sensing capacities of pure and Al-doped ZnO nanoparticles towards methanol (CH₃OH), toluene (C₇H₈), ethanol (C₂H₅OH), and ammonia (NH₃) were investigated at room temperature. The one-wt% Al-doped ZnO sensor demonstrated an ultrafast response and recovery times at one ppm compared to other AZO-based sensors towards NH₃.

Address correspondence to E-mail: bindu1024@gmail.com; nululathadevi@gmail.com

1 Introduction

ZnO is a promising II–IV semiconductor at ambient temperature, with a direct bandgap of 3.37 eV and a significant excitation binding energy of 60 MeV [1]. ZnO nanostructures are utilised in optoelectronics, photocatalysis, solar cells, purification, electrical contacts for light-emitting diodes, separation, and chemical sensors. The microwave induced [1], wet chemical [2], sol–gel [3], hydrothermal [4], soft chemical [5], chemical vapour phase [6], and magnetron sputtering [7] techniques are the most common methods for producing ZnO nanoparticles. The co-precipitation technique was used in this experiment. It is the most widely used and accessible methodology due to its simple experimental approach and low cost, making it economically advantageous. When pure semiconductor capabilities are insufficient to meet the demands of the desired applications, one of the most effective approaches to improve semiconductor performance is doping with appropriate elements. ZnO has been doped with aluminium [8], gallium [9, 10], cadmium [11], copper [12], and other materials to optimise its optical, electrical, and physical properties. In the literature, Indeed, various publications have proposed chemoresistive sensors based on WO_3 [13], SnO_2 [14], Co_3O_4 [15], and ZnO [16] that have been investigated for the detection of VOCs. ZnO is particularly intriguing due to its simplicity of fabrication and strong chemical and thermal stability [17], particularly when doped with diverse dopants due to its chemical structure, high sensitivity, quick response and recovery time, and selectivity to VOCs and flammable gases [18]. Fe-doped ZnO/graphene oxide nanocomposite is reported for formaldehyde sensing at 5 ppm with a working temperature of 120 °C [19]. As a consequence of the doping of Li to ZnO, the working temperature of the sensor has been decreased from 500 °C to 150 °C for hydrogen detection at a flow rate of 50 SCCM [20]. In a few reports, graphene/ZnO nanocomposites were used for co-sensing at 10 ppm at room temperature [21]. Yoo, R., Güntner, et al. [8] used a hydrothermal technique to create Al-doped ZnO and discovered acetone gas detection operating between 250 and 500 °C. The sensing response increases up to 450 °C and decreases towards 500 °C due to the desorption of adsorbed oxygen from the surface of ZnO nanoparticles. Finally, the lowest acetone

concentration was reported at 450 °C, at 0.1 ppm. R. Sankar Ganesh et al. [22] used a hydrothermal technique to create Cu-doped ZnO and reported the best lower contraction of NH_3 of 10 ppm at 150 °C. S. Brahma et al. [23] employed a hydrothermal method to produce a Cd-doped ZnO and reported superior specific detection of NH_3 over NO_2 and H_2S at 25 °C.

Al doping has been found to improve sensor sensitivity to gas molecules by reducing the thermal conductivity of ZnO semiconductors. The current study aims to improve our understanding of the influence of Al doping on the optical and structural characteristics of ZnO, thereby improving its gas-sensing capabilities. According to the literature, the synthesis processes and experimental conditions have a significant influence on the gas-sensing properties of nanoparticles, including particle size, shape, variations in the optical band gap, surface area, resistivity, and other properties [24].

Novel gas sensors with excellent detection capabilities and functioning at room temperature are attractive owing to their lower power consumption, better reliability, and long-term consistency. The operating temperature governs the reaction kinetics, conductivity, and charge carrier mobility and significantly influences the gas detection abilities of ZnO-based gas sensors [25]. The surface redox process requires sufficient heat energy to overcome the activation energy barrier, optimise reaction kinetics, and enable sensor measurements. However, high temperatures result in energy waste, which contradicts our society's energy conservation and emission reduction goals and restricts its wide application [26]. Furthermore, gas explosions are rare because they are flammable and have low ignition points under normal conditions. Moreover, high-temperature operations create sensor instability, which results in inaccurate readings. As a result, the operating temperature of ZnO-based gas sensors must be urgently lowered. Many researchers have attempted to reduce the operating temperature to room temperature. The most advantageous methods based on pure ZnO nanostructures include surface modification, additive doping, and the use of ZnO-loaded carbon composite materials.

The present study aims to detect lower concentrations of the target gas (NH_3), even at room temperature, using an additive doping technique with a suitable element. Ammonia has been designated as a

dangerous material by the National Fire Protection Association (NFPA) in the USA, making it a chemical with significant health risks. Legal restrictions and exposure duration determine the limits of human ammonia exposure. There are severe repercussions of exposure to quantities exceeding the limit of 25–50 ppm. Ammonia levels in the body have long been associated with difficulties and can induce significant illnesses, such as chronic renal disease, bleeding ulcers, and most recently, COVID-19. Elevated blood urea nitrogen levels in the body cause poor liver and renal function, resulting in excessive ammonia levels in the mouth, nose, and skin. These biomarkers enable a prospective screening approach for regular, non-invasive monitoring of the disorders under investigation. Currently, there are no alternatives for real-time, continuous, and non-invasive screening of these disorders. A vapour-phase thermodynamic sensing platform can be used as a health screening process to detect ammonia levels [27–29]. Many applications, such as human and fish respiration monitoring and fire detection, require a quick diagnosis of dynamic changes in NH_3 gas concentration with high sensitivity, fast response, and recovery times. Aquatic contamination and fish poisoning can be caused by ammonia. Acute exposure to ammonia can destroy juvenile common snook gills and alter blood cell counts, hematocrit, and glucose levels, leading to mass death under adverse aquaculture conditions. The threshold levels for NH_3 tolerance and mortality rate in the aquaculture industry are above 3 ppm at room temperature [27, 30, 31]. Ammonia levels in fish tanks and the mortality rate of fish can be controlled even at ambient temperatures [32–34].

Here, we discuss the impact of Al dopant on optical gas sensing and the ZnO nanostructure of nanoparticles for NH_3 detection. The co-precipitation method was used to fabricate both pure and Al-doped ZnO. Owing to its simple experimental technique and low cost, which make it economically viable, it is the most extensively used and accessible methodology. Additionally, we examined the physical and chemical properties, such as crystalline phase, bandgap, specific surface area, and density of porosity, via N_2 adsorption of pure and Al-doped ZnO nanoparticles in order to better understand the various sensing capabilities. In the current study, all Al-doped ZnO samples could detect NH_3 at lower concentrations, between 2 ppm and 1 ppm. As a

result, the Al-doped ZnO ammonia sensor (current work) can pre-warn at low ammonia concentrations to monitor the aforementioned functions.

2 Experimental

2.1 Materials

Pure and Al-doped ZnO nanoparticles were synthesised using $\text{Zn}(\text{NO}_3)_2 \cdot 6\text{H}_2\text{O}$, $\text{Al}(\text{NO}_3)_3 \cdot 9\text{H}_2\text{O}$, NaOH, and PVP M.W. 40,000. Double deionised water and ethanol were used as the solvents for the preparation process. All chemicals were of analytical grade and were used directly.

2.1.1 Synthesis of Al-loaded zinc oxide

$\text{Zn}(\text{NO}_3)_2 \cdot 6\text{H}_2\text{O}$ (0.2 M) was dissolved in ethanol (10 mL) at room temperature. The solution was agitated until it became transparent. A 0.06-M PVP solution was added dropwise to the above solution and stirred for approximately 10 min. A NaOH aqueous solution (0.5 M) was added dropwise to the mixed sol to obtain a white precipitate. After that, 0.02 M of $\text{Al}(\text{NO}_3)_3 \cdot 9\text{H}_2\text{O}$ was added dropwise and stirred continuously for 30 min. The combined solution was transferred to a glass container with a tight lid and kept in a hot-air oven at 100 °C for 4 h. Then, a white precipitate settled at the bottom and was washed 5–6 times with double deionised water to avoid the formation of chemical species during the synthesis process. The sample was dried for a week at room temperature before being finely powdered using a mortar and pestle. The collected sample was calcined at 300 °C for three hours in a muffle furnace. A similar method was used with 2 and 4 wt%. The samples were labelled 1 wt% as A-ZO1, 2 wt% as A-ZO2, and 4 wt% as A-ZO4.

2.1.2 Measurement of gas sensing

We mixed ZnO and AZO nanoparticles separately with methanol and coated them on a cleaned glass substrate (Blue Star, India) for gas-sensing assessments. The conductive silver paste was applied to both ends and dried for an hour at 100 °C in a hot-air oven to create ohmic connections on the glass substrate surface. Electrical connections were attached from the gas chamber to the desktop and

interconnected with a high-resistance electrometer (6517 B, USA). A chromatographic syringe was used to inject an appropriate amount (ppm) of the target gas into the metallic tube connected to a heater inside the gas chamber. The Keithley electrometer detected an abrupt change in the resistance to the baseline value because the sensor was exposed to the target gas, resistance of the sensor in the presence of air (R_a), and resistance in the presence of target gas (R_g).

3 Results and discussion

3.1 Determination of lattice parameters and structural properties

Figure 1 shows the XRD patterns of the ZnO and Al-doped ZnO nanoparticles calcined at 300 °C for three hours. The ZnO and AZO samples exhibited a characteristic hexagonal structure with a Wurtzite ZnO crystalline phase with 2θ values of 31.71°, 34.37°, 36.19°, 47.51°, 56.57°, 62.85°, 66.01°, 67.96°, 69.07°, 72.65°, and 77.11°, corresponding to the Miller reflections of (100), (002), (101), (102), (110), (103), (200), (112), (201), (004), and (202), respectively (JCPDS card number 036-1451) [35]. The samples

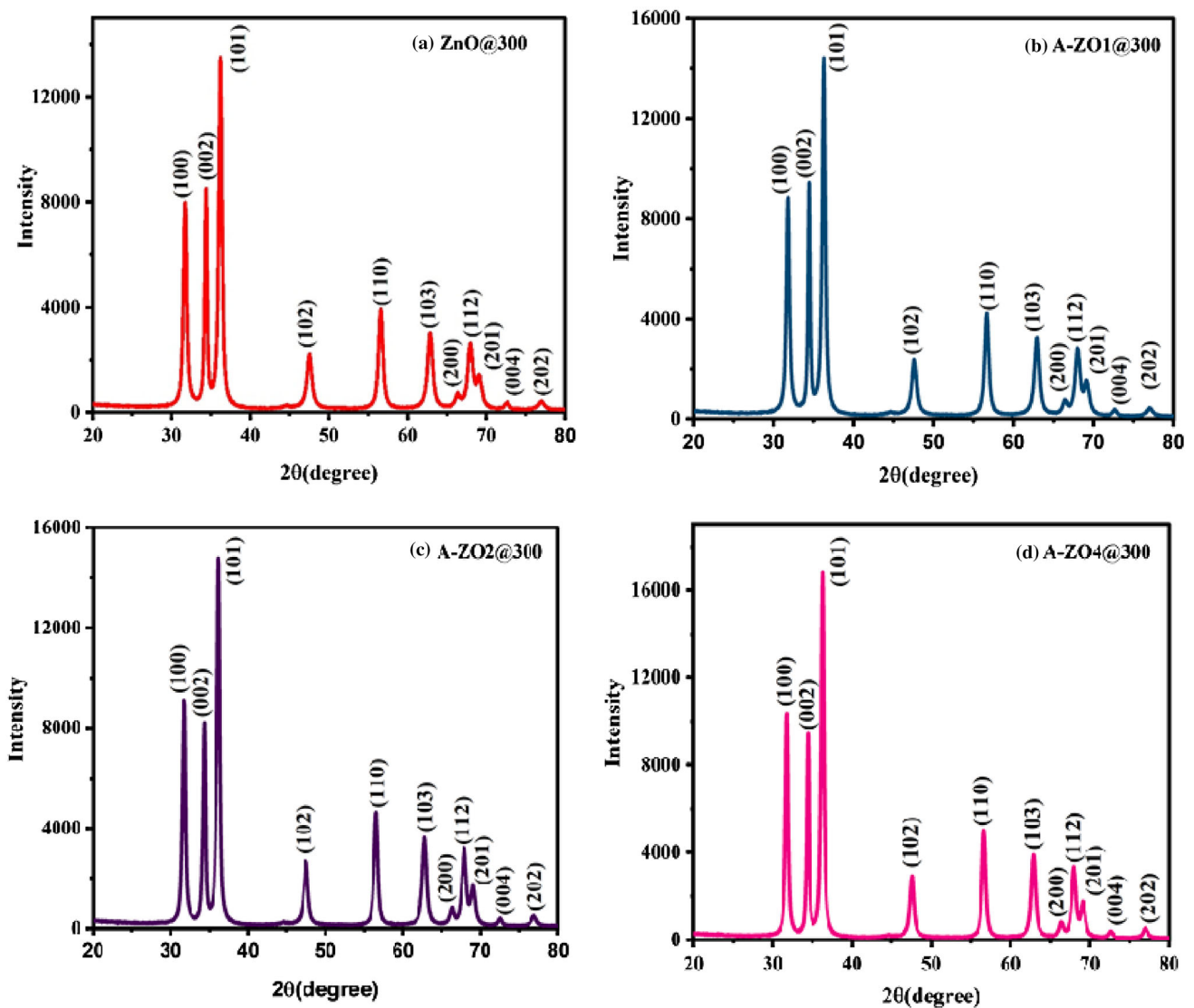


Fig. 1 a–d XRD pattern of Al-doped ZnO nanoparticles with various Al percentages

exhibited a hexagonal Wurtzite crystal phase of ZnO. No additional peaks of Al₂O₃ or Zn (OH)₂ were detected, confirming that Al³⁺ was incorporated into the ZnO host lattice. Overall, the intensity of AZO diffraction peaks increased rapidly as Al doping concentration increased (1–4 wt%), which was especially visible for the (101) peak, implying an increase in crystallite size. These findings suggest that the presence of Al atoms in the ZnO lattice enhances crystal quality. The diffraction peaks with miller indices (100) and (200) of the A-ZO1 and A-ZO4 samples are shifted towards higher 2θ values, as shown in Fig. 1a–d, reflecting a decrease in lattice parameters ‘a’ and ‘c’ values. However, for the A-ZO2 sample, the same peaks are shifted towards lower 2θ values, indicating an increase in lattice parameters “a” and “c” shown in Table 1. The Scherrer formula is employed to investigate crystallite size [36].

$$D = \frac{k\lambda}{\beta \cos(\theta)}, \tag{1}$$

where D is the average crystallite size, λ is the x-ray wavelength, β is the width of the x-ray peak on the 2θ axis, normally measured as the full width at half maximum (FWHM) after the error due to instrumental broadening has been properly corrected (subtraction of variances), θ is the Bragg angle, and K is the so-called Scherrer constant [37]. The crystallite sizes investigated are listed in Table 1.

For pure and Al-doped ZnO, the interplanar spacing, “u” parameter, and lattice parameters “a” and “c” are determined [35, 38] and tabulated in Table 1. Slight variations in unit cell volume, Zn–O bond length (L), atomic packing factor, and ‘u’ parameter were observed. It might be due to the slight shifting of ‘2θ’ caused by adding Al to ZnO. Table 1 shows that the lattice parameters of pure ZnO are 3.257 Å and 5.216 Å. The variation in the lattice parameters might be attributed to the lower ionic radii of Al³⁺ (0.53) being replaced by the Zn²⁺ (0.74) site in the ZnO lattice [35]. However, for the A-ZO2 sample, the same peaks are shifted towards lower 2θ values, indicating an increase in lattice parameters “a” and “c” shown in Table 1. The size of the crystallites gradually increased when Al atoms were incorporated into the ZnO lattice because of the enhanced crystalline quality and dopant atom segregation on the ZnO surface [39].

3.2 Scanning electron microscopy (SEM)

Figure 2a–d reports ZnO and AZO nanoparticles with a flower-like morphology [40, 41]. The dimensions of the nanopetal may vary depending on the doping concentration. However, the grain shape is inconsistent across all samples and is affected by doping. The incorporation of Al atoms into the ZnO host lattice is vital for crystallite aggregation. [35]. The variations in grain size are probably the result of aluminium doping. The effective surface area significantly increased owing to the flower-like

Table 1 Structural parameters of pure and Al-doped ZnO nanoparticles

Sample	Crystallite Size (nm)	(hkl)	a(A°)	c(A°)	c/a	u parameter	Cell volume V(A°) ³	Bond Length L (A°)	Inter Planar Spacing d (A°)	A.P.F. (%)
ZnO	14.14	(1 0 0) (0 0 2)	3.257	5.216	1.6015	0.3799	47.92	1.982	1.863	75.469
A-ZO1	14.82 75.457	(1 0 0) (0 0 2)	3.249	5.204	1.6017	0.3799	47.57	1.977	1.858	
A-ZO2	15.74 75.458	(1 0 0) (0 0 2)	3.259	5.220	1.6017	0.3799	48.00	1.983	1.864	
A-ZO4	17.49 75.475	(1 0 0) (0 0 2)	3.251	5.206	1.6013	0.3799	47.65	1.978	1.859	

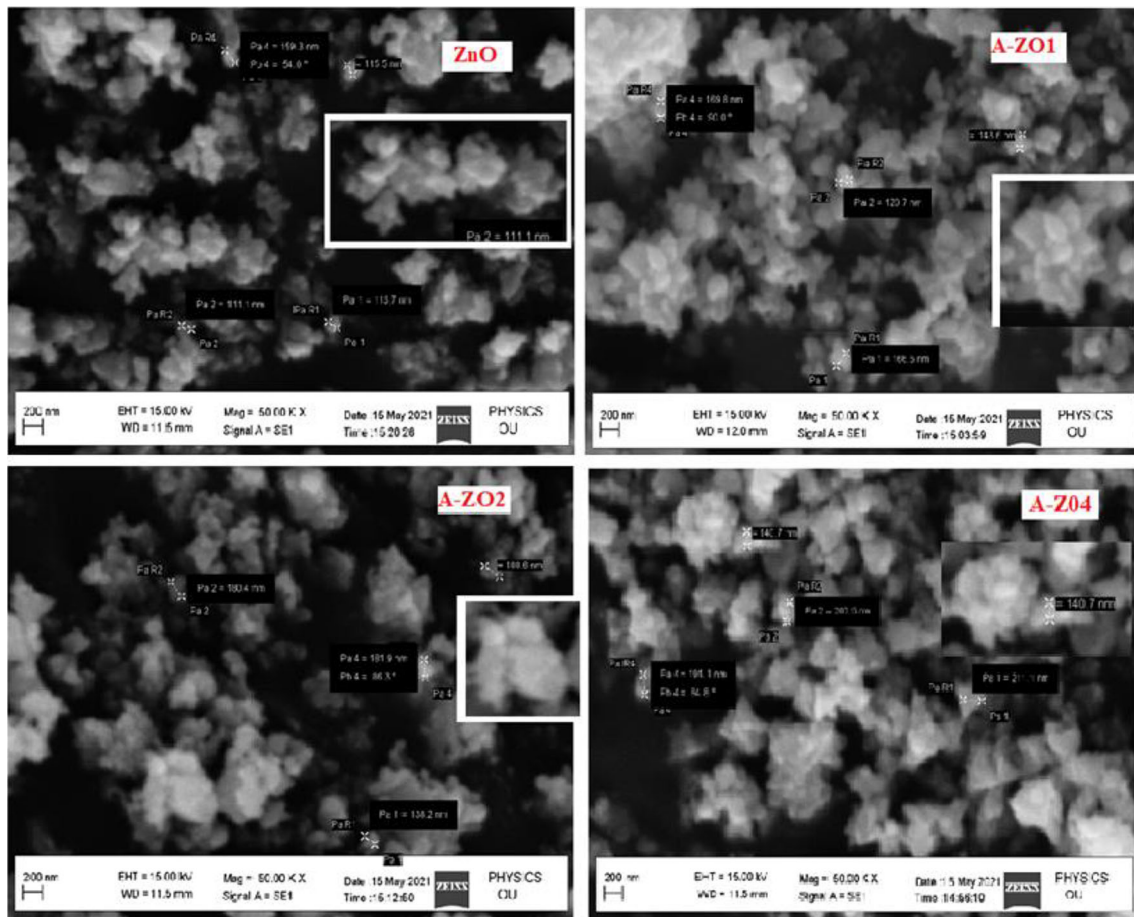


Fig. 2 SEM images of pure and Al-doped ZnO nanoparticles

morphology, which enhanced the sensing capabilities. The ZnO and Al-doped ZnO nanoparticles have shown nanostructures and the average particle size is obtained from Fig. 2a ZnO: 124.9 nm, b A-ZO1: 150.2 nm, c A-ZO2 172.3 nm, and d A-ZO4:186.6 nm. (The inset images were cropped from similar SEM images, which all exhibit flower-like morphology)

3.3 Energy-dispersive spectroscopy (EDS)

The EDS results of ZnO and Al-doped ZnO nanoparticles calcined at 300 °C are shown in Fig. 3a–d. EDS analysis is used to determine the components that are present in the samples. It is a semi-quantitative approach for calculating the proportion of each constituent. The atomic proportions of Zn, Al, and O are presented in Table 2. The abscissa represents the ionisation energy and the ordinate denotes the count. The greater the count of a specific element, the more prevalent it was at that

time. The EDS spectrum of Al-doped ZnO revealed the presence of dopant elements in Zn, O, and Al; there are a lack of further impurities in the ZnO host lattice.

3.4 FTIR (Fourier transform infrared spectroscopy)

FTIR was used to determine the functional groups contained in the pure and aluminium-doped ZnO samples in the wavenumber band of 400–4000 cm^{-1} under ambient conditions to provide more insight into the structure of the sample, as displayed in Fig. 4. The FTIR method is utilised for the sample's structural examination. It enables us to determine the various interactions between those elements (possible bonds). The pure ZnO peak at 500 cm^{-1} is ascribed to the stretching mode [42–44]. As the doping increases, this peak shifts towards higher frequencies,

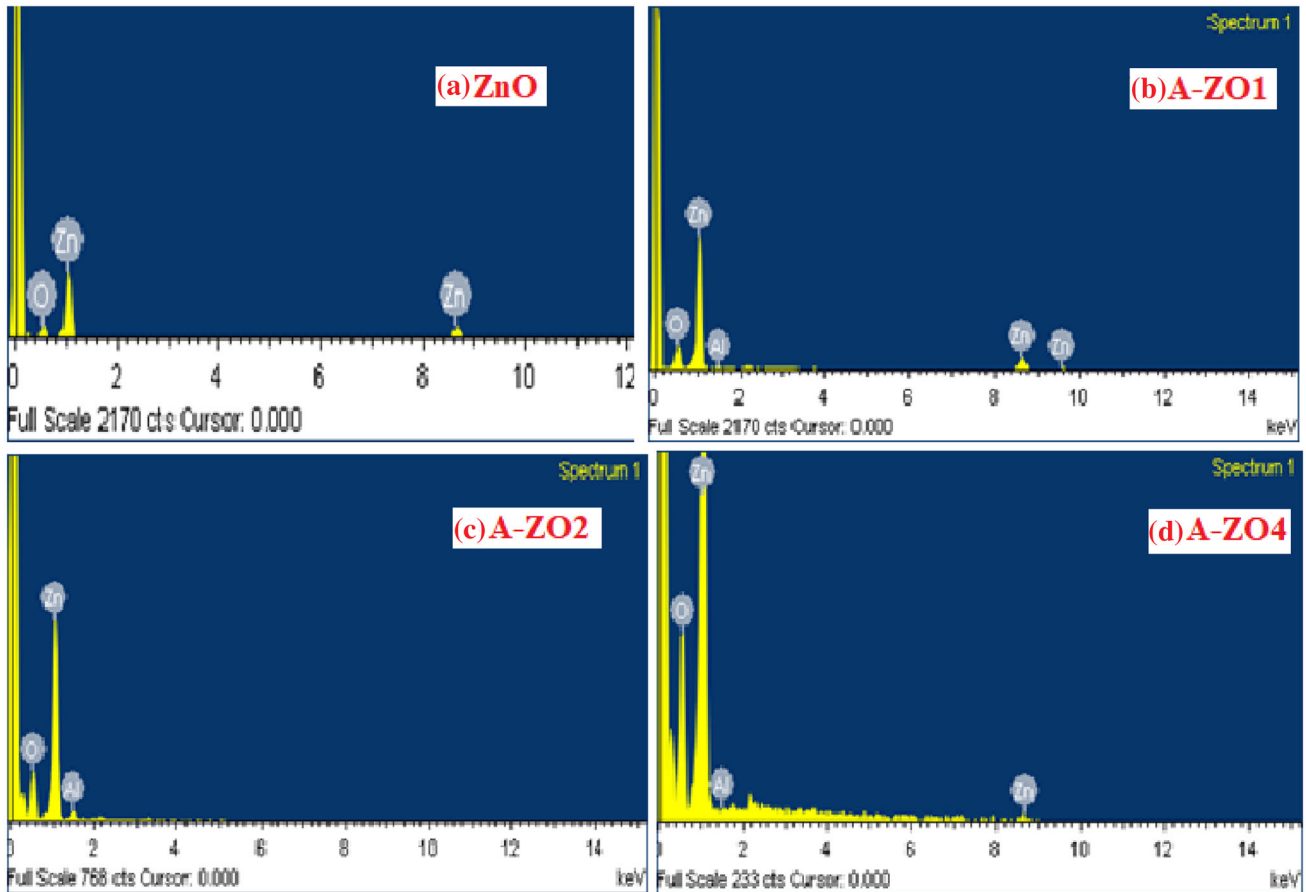


Fig. 3 a–d EDS of the various percentage of Al-doped ZnO

Table 2 The percentages of Zn, O, and Al atoms in each sample

Sample	Zn (atomic%)	O (atomic %)	Al (atomic%)
ZnO	49.62	50.38	–
A-ZO1	46.79	52.27	0.94
A-ZO2	45.80	52.68	1.52
A-ZO4	42.66	53.83	3.51

indicating the possible substitution of Al^{3+} ions and internal strain acting on the size of the ZnO nanocrystallites, reducing the Zn–O bond length. This finding indicates that Al^{3+} ions occupy Zn^{2+} positions in the ZnO host lattice [45]. The absorption peak at 2900 cm^{-1} is caused by the organic surfactant used in the production process, which causes C–H bond bending vibrations [46]. The peak shows the hydroxyl residue owing to ambient moisture at 1590 cm^{-1} . The peak at 2350 cm^{-1} indicates that CO_2 molecules were present in the air. Hence, the

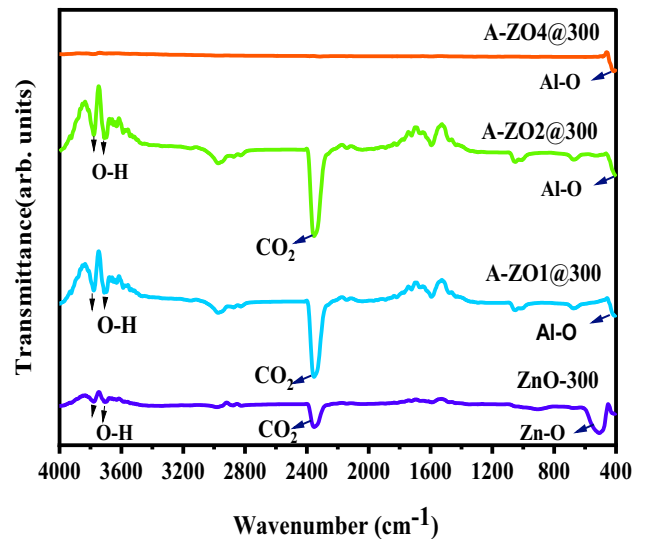


Fig. 4 FTIR analysis of pure and Al-doped ZnO nanoparticles at various doping concentrations

nanoparticles trapped CO₂ from the atmosphere during FTIR [47, 48]. The peaks at 3700 cm⁻¹ and 3800 cm⁻¹ correspond to O–H stretching modes [49].

3.5 Evaluation of optical bandgap from UV-DRS

UV diffuse reflectance spectroscopy (UV-DRS) was used to analyse the energy bandgap of zinc oxide and aluminium-doped ZnO samples. The energy gap, or optical bandgap, is the energy required for an electron to move from the valence band to the conduction band. ZnO has a direct bandgap of 3.37 eV. The following equation suggests the relation between optical bandgap (E_g) and the Kubelka–Munk function $F(R)$.

$$(F(R)h\nu)^2 = h\nu - E_g, \quad (2)$$

where $F(R)$ represents the Kubelka–Munk function and $h\nu$ is the incident photon energy [50–52]. Figure 5 displays the variation in the Kubelka–Munk function $(F(R)h\nu)^2$ of the samples with photon energy ($h\nu$). The

linear extrapolation of the Kubelka–Munk function on the X-axis was used to determine the optical band gap. The optical bandgaps of ZnO, A-ZO1, A-ZO2, and A-ZO4 are 3.277, 3.240, 3.234, and 3.210 eV, respectively. Here, the optical bandgap decreased as the doping concentration increased owing to the size parameter, confirming the effect of the sensing mechanism. According to the XRD results, the increase in crystallite size and enhanced crystal quality may be responsible for the low-energy bandgap of the doped sample. In addition, the decline in the optical bandgap after Al doping implies a deterioration of the quantum confinement effect in the ZnO nanoparticles and also due to the strong “sp–d” exchange interaction between the “sp electrons” of ZnO and the “d” electrons of Al ions, which substitute Zn + 2 ions [53]. This finding is consistent with those of other published studies [54]. Furthermore, Caglar et al. [55] reported that Al doping results in narrowing bandgap energy, which is due to an increase in the number of electrons at the conduction band edge and the generation of new recombination centres with low emission energy.

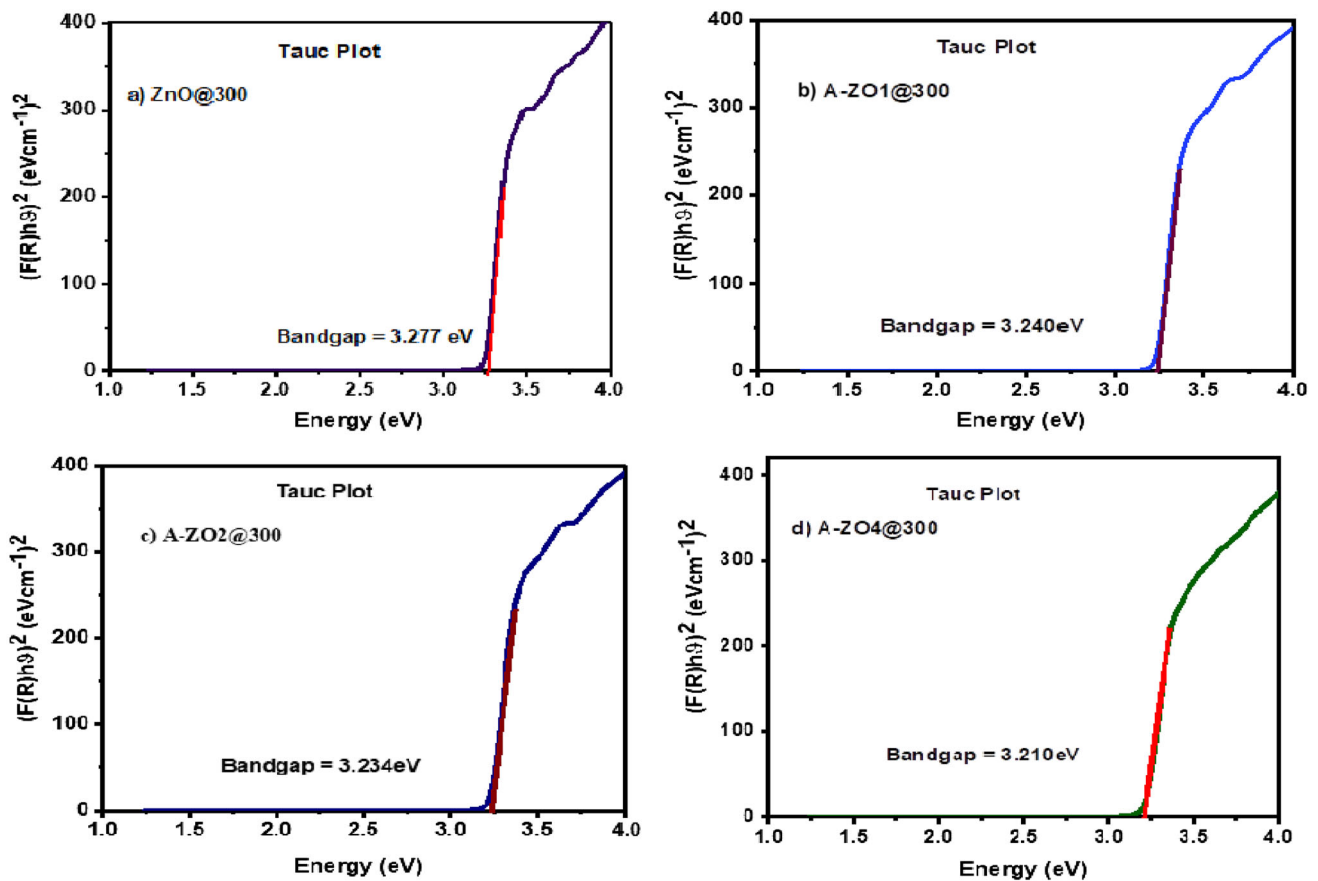


Fig. 5 a–d $(F(R)h\nu)^2$ versus Energy for Al-loaded ZnO nanoparticles with varying concentrations of Al

3.6 AFM (Atomic Force Microscopy)

Topological characterisation is essential for the present gas-sensing properties. AFM is beneficial for estimating the doping contribution to the crystallite synthesis process and for assessing the surface nature of nanoparticles. The changes in surface morphology and roughness caused by doping were revealed by the AFM investigation [56]. AFM images of the pure and Al-loaded ZnO samples are shown in Fig. 6a–d. The image scanning area was set to $1\ \mu\text{m} \times 1\ \mu\text{m}$ and exhibited a uniform surface with bud-like grains covering the ZnO surface. The AFM results revealed that the surface roughness corresponded to the scanned region of the pure and Al-doped ZnO nanoparticles. The surface roughness decreased as the Al doping increased and was measured for the ZnO-182 nm, A-ZO1-230 nm, A-ZO2-131 nm, and A-ZO4-43 nm. Surface roughness is high for A-ZO1, implying good sensing characteristics. Roughness values are preferred for various

applications, and a decrease in surface roughness diminishes surface adsorption and decreases the probability of oxygen adhering to the surface [57–59].

3.7 BET surface area analysis of the as-obtained ZnO precursor and AZO nanoparticles

The surface area, pore volume, and average diameter of the obtained ZnO and A-ZO samples annealed for two hours determined N_2 adsorption. Figure 7a–d shows the N_2 adsorption–desorption isotherms of the ZnO precursor and the A-ZO1, A-ZO2, and A-ZO4 samples annealed at $300\ ^\circ\text{C}$. Figure 7 displays type-IV isotherm according to the IUPAC classification [60, 61]. Barrett–Joyner–Halenda’s (BJH) analysis was used to determine the pore size distribution. The average pore diameter varies from 8.34 to 7 nm, to less than 50 nm, and is compatible with a good mesoporous material [62, 63].

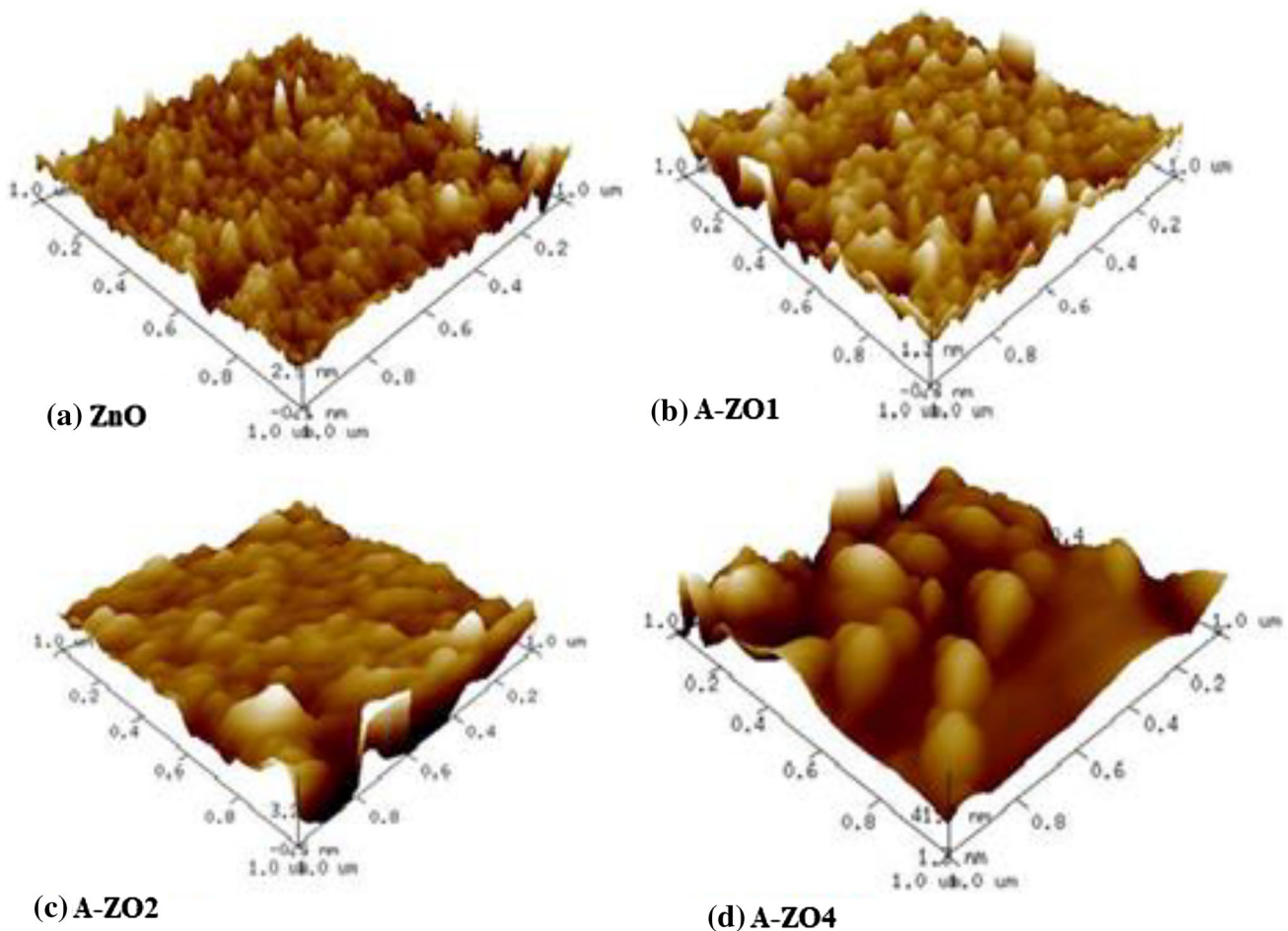


Fig. 6 a–d Atomic force microscopy of pure and Al-loaded ZnO samples with different concentrations

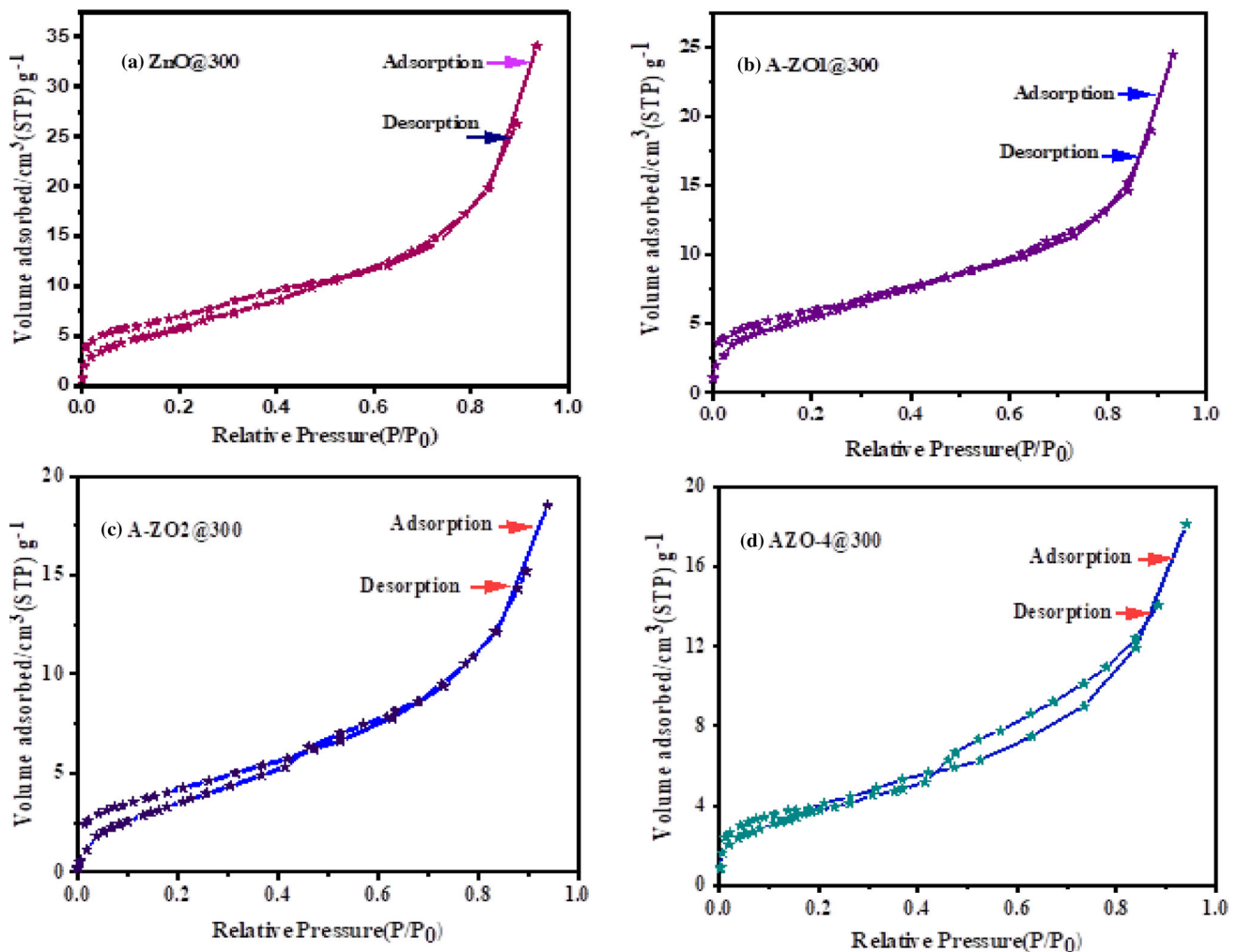


Fig. 7 a–d Adsorption–desorption isotherms

The surface area and pore volume decline were caused by pore collapse, subsequent nanoparticle aggregation, and oxygen adsorption. The high A-ZO1's specific surface area and pore volume can provide abundant surface active sites. Additionally, it enables easy charge carrier transmission, resulting in improved NH₃ sensing properties at lower concentrations. Table 3 shows the surface areas, pore volumes, and average diameters of the ZnO and A-ZO samples.

4 Selectivity & sensing mechanism

According to the XRD results, A-ZO₁ has a smaller crystallite size, broad bandgap from UV-DRS, high surface roughness based on AFM studies, high

surface area, and the smallest pore volume from BET analysis compared to the other AZO samples. As a result, it was optimised for gas sensing properties, along with pure ZnO. Figure 8 illustrates the histograms showing the responses of the optimised sensors towards different gases, and it is found that there is the highest response towards 50 ppm of NH₃ at ambient temperature. The high surface-to-volume ratios of ZnO and A-ZO₁ are responsible for their remarkable responses. The A-ZO₁ sensor employs a chemi-resistive technique to identify VOC gases, including methanol, ethanol, and toluene.

The reaction mechanism is based on the variation in the resistance of the sensing layer upon exposure to the target gas. The NH₃ sensing mechanism is detailed below. Adsorption is characterised by surface imperfections. Oxygen adsorption occurs if a

Table 3 Report of BET analysis for pure and Al-doped ZnO samples

S.No.	Sample code	BET-specific surface area (m ² /g)	BJH mean pore diameter (nm)	Total pore volume (P/P ₀) (cm ³ g ⁻¹)
1	ZnO-300	25.274	8.34	0.053
2	A-ZO1	21.627	7.00	0.038
3	A-ZO2	15.281	7.50	0.029
4	A-ZO4	14.755	7.60	0.028

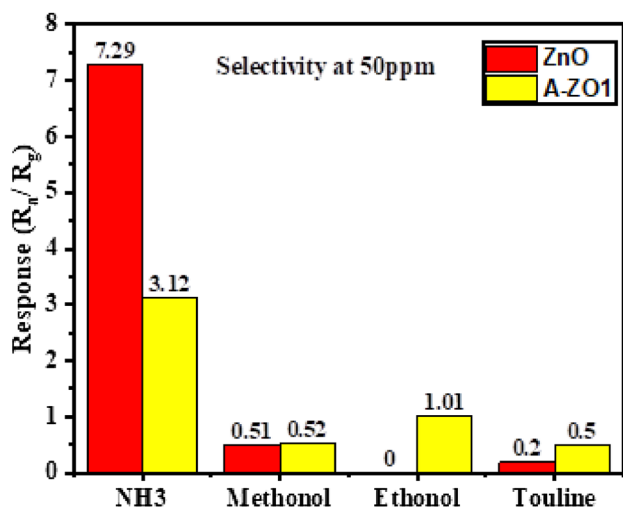
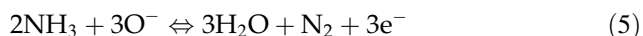
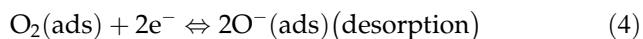
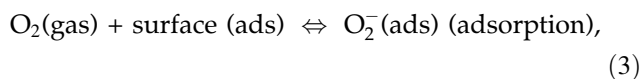


Fig. 8 Selectivity of undoped and Al-doped ZnO samples

material’s surface comes into contact with air. The adsorbed oxygen absorbs electrons from the sample surface, forming ionic species such as O²⁻ and O⁻ on the surface. The kinetic reactions before and after the target gas were as follows:



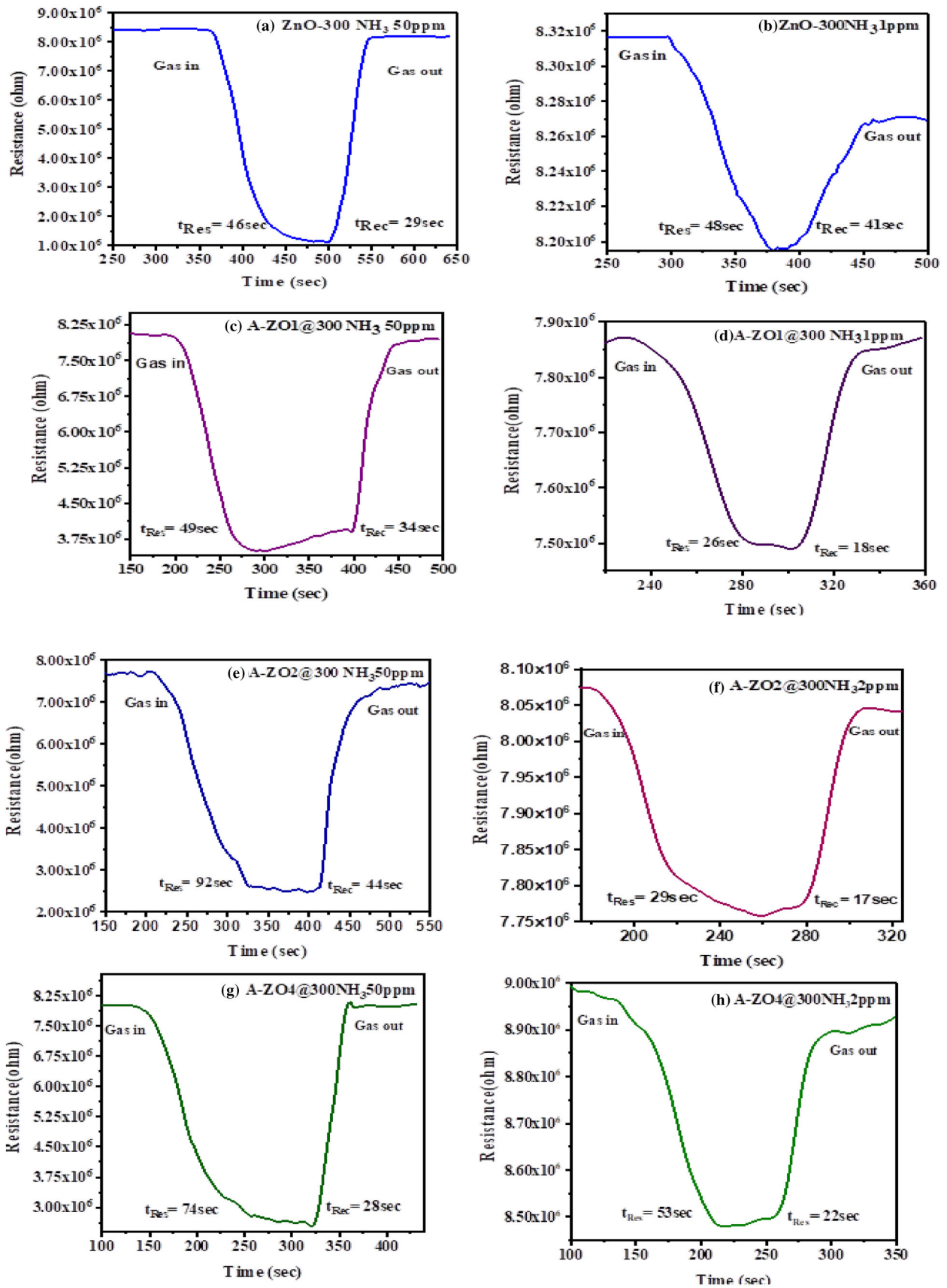
These oxygen species help to create a depletion layer on the ZnO surface. Consequently, the electron density increased. When the sensor was exposed to NH₃ as a reducing gas NH₃ molecules reacted with oxygen ions that subsequently released the electrons back to the conduction band and narrowed the depletion layer. The equation describes the reaction’s electron release (5). This raises the electrons, resulting in a decrease in the surface resistance of AZO. The sensing layer determines the relevant gas sensitivity

when the adsorbed oxygen reacts with the target gas molecules when aluminium is added as a dopant, which helps to complete the ZnO structure, allowing more oxygen to be adsorbed to increase the number of active sites on the surface. Consequently, the resistivity decreases, increasing the surface area and enhancing the sensing performance, even at lower concentrations of the target gas. This is possibly due to the high porosity of the sensing material and smaller crystallite size.

The present investigations focused on detecting lower concentrations of ammonia gas at room temperature. In the present study, all the pure and AZO samples had excellent sensing abilities at room temperature, especially A-ZO1, demonstrating extraordinary sensing properties towards lower concentrations of NH₃. This is because A-ZO1 has a smaller size, higher surface area, smaller pore diameter, and smaller pore volume, which helps to increase the number of active sites and enables ultrafast detection at lower concentrations, even as low as 1 ppm.

The response and recovery times of the sensor decreased when the Al doping concentration increased from 1 to 4 wt% at room temperature, as depicted in Fig. 9a–h, indicating the doping influence on the gas-sensing characteristics of ZnO nanoparticles. The chemi-resistive technique is based on changes in the electrical resistivity of the samples.

This is an outcome of the chemical interactions between the surface complexes, such as O⁻ and O²⁻ gaseous molecules. The ammonia gas-sensing abilities of pure ZnO and AZO nanoparticles were investigated at ambient temperature. The results revealed that ZnO and A-ZO1-based sensors have outstanding gas-sensing properties towards lower concentrations of 1 ppm. This is due to the presence of Al³⁺ at the Zn²⁺ lattice site, increased surface area, and smaller crystallite size compared to those of the remaining AZO samples. Figure 9d shows that



◀ **Fig. 9 a–h** The NH_3 response and recovery times of undoped and Al-doped ZnO sensors at ambient temperature for various concentrations

A-ZO1 yields ultrafast response (26 s) and recovery (18 s) times at one ppm (parts per million). The response and recovery times are necessary parameters for evaluating the potential applications of the sensor. This is due to the small mean pore diameter and porosity density in the BET analysis. They are also due to the smaller crystallite size from the Scherrer formula and the significant surface roughness from AFM. A-ZO2 and A-ZO4 also demonstrated good sensing performances at 2-ppm NH_3 . This can be attributed to the equivalent BET surface area, BJH mean pore diameter, and pore volume.

Table 4 shows comparison of the sensing characteristics of various ZnO dopants, morphologies at different working temperatures, and lower concentrations of target gases described in the literature with the current work. J. Mohanraj et al. [64], G. Alexieva et al. [65], and F. Shu Xing et al. [66] demonstrated that Al-doped ZnO thin film, Al-doped carbon nanofiber, and Al-doped ZnO nanoparticles exhibited sensing performance towards NH_3 as low as 100 ppm, 50 ppm, and 10 ppm at ambient temperature. H. A. Varudkar et al. [53] synthesised Al-doped ZnO nanoparticles by the co-precipitation method and obtained a spherical morphology; they reported sensing performance towards NH_3 as low as 10 ppm at room temperature. K. R. Devi et al. [67] used the SILAR approach to synthesise Al-doped ZnO nanoparticles with a nanowire structure; they reported NH_3 sensing performance as low as 100 ppm at ambient temperature. L. H. Kathwate et al. [68] employed spray pyrolysis to produce Al-doped ZnO nanoparticles with NH_3 sensing capability as low as 25 ppm at 100 °C. A. Jagan Mohan Reddy et al. [69] reported that hydrothermal Al-doped ZnO nanoparticles with NO_2 sensing capabilities are as low as 1 ppm at 240 °C. P.S. Kohle et al. [70] and A. Handan et al. [71] used spray pyrolysis and spin coating techniques to develop Al-doped ZnO nanoparticles with H_2S and NH_3 sensing capabilities as low as 600 ppm at 200 °C in ambient temperatures. P. Madhukar et al. [14] employed sol–gel procedures to create Al + ZnO/CuO nanoparticles with NH_3 detection capabilities as low as 500 ppm at ambient temperatures. Sol–gel techniques were used by A.

Koo, C. R. Yoo et al. [14], and G. V. Colibaba et al. [6] to make Al + ZnO thin films and Al-doped nanoparticles with acetone detection capabilities as low as 10 and 1 ppm at 250 °C–500 °C and 450 °C, respectively.

Here, significant progress has been achieved in recent years towards lowering the operating temperature of ZnO-based gas sensors to room temperature. Table 4 demonstrates that A-ZO1 nanoparticles have a high sensitivity to ammonia at ambient temperature compared to the literature. A remarkable enhanced feature has been noticed in the present work: quick response and recovery times and the lowest concentration of 1 ppm of NH_3 detected at room temperature. This finding is attributable to the density of oxygen vacancies, which results in a higher number of adsorbed oxygen ions on the surface of ZnO that can react with NH_3 . To the best of our knowledge, no other researcher has shown that low concentration at room temperature yields the best outcomes.

5 Conclusion

In the present report, we present sensor-based AZO nanoparticles synthesised by the co-precipitation method. The incorporation of Al ions into the ZnO structure has been confirmed by XRD, EDX, and FTIR. The morphological analysis approves the development of flower-like structures, which is favourable for gas sensing. The evaluated energy gap varied from 3.240 to 3.210 eV as Al doping increased due to crystallite size. The detection of NH_3 gas was studied based on a lower gas concentration. It has been discovered that the materials' higher roughness, smaller pore volume, and smaller crystallite sizes all enhance the A-ZO1 sensing capabilities. Furthermore, when compared to other AZO samples, AZO-1 has demonstrated faster response and recovery times at room temperature; the response time was 26 s; and the recovery time was 18 s. Hence, the prepared nanoparticles were suitable for gas sensors at room temperature and optoelectronic device applications at low gas concentrations. These findings show that the NH_3 gas sensor has enormous industrial and environmental monitoring potential. The sensor has significant potential for non-invasive breath detection in patients with gastrointestinal illnesses and other medical domains to identify diabetes, renal failure,

Table 4 Comparison between the present work and literature on the sensing properties of various ZnO dopants, morphologies at different working temperatures, and lower concentrations of target gases

S.no	Doped material with ZnO	Preparation Technique	Morphology	Target gas	Operating Temperature	Lower Concentration of the gas (ppm)	References
1	ZnO/CuO Nanoparticle	Hydrothermal	Flower like	NH ₃	R.T	5	[64]
2	Al + ZnO thin film	Electrochemical	Nanorods	NH ₃	R.T	100	[65]
3	ZnO + Carbon nanofiber	Electrospinning, pre-oxidation, oxidation, and carbonization	nanofiber	NH ₃	R.T	50	[66]
4	Al + ZnO Nanoparticles	Co-precipitation	Sphere shaped	NH ₃	R.T	10	[53]
5	Al + ZnO thin film	SILAR	Nanowire	NH ₃	R.T	100	[67]
6	Al + ZnO thin film	Spray pyrolysis	Nano particles	NH ₃	100 °C	25	[68]
7	Al + ZnO nanoparticles	Hydrothermal	hierarchical narcissus	NO ₂	240 °C	1	[69]
8	Al + ZnO thin film	Spray pyrolysis	Nanoflakes	H ₂ S	200 °C	600	[70]
9	Al + ZnO thin film	Sol-gel spin coating	cluster structure of nanosized particles	NH ₃	R.T	600	[71]
10	Al + ZnO/CuO Nanoparticles	Sol-gel	Nanograins	NH ₃	R.T	500	[14]
11	Al + ZnO thin film	Flame Spray pyrolysis	Spherical to rod like	Acetone	250–500 °C	10	[7]
12	Al + ZnO Nanoparticle	Hydrothermal	Spherical to rod like	Acetone	450 °C	1	[6]
13	Al + ZnO Nanoparticles	Co-precipitation	Nanoflower like	NH ₃	Room Temperature	1	Present work

R.T = Room temperature

and ketoacidosis due to its unique characteristics of good sensitivity to ammonia at room temperature and remarkable flexibility.

Acknowledgements

The authors thank our colleagues Dr. I. Sirisha and Mrs. M. Sheetal Reddy for editing the English in this manuscript. The authors are grateful to the administration and principal of S.I.E.T., T.K.R.C.E.T., and C.M.R. Technical Campus for providing the required infrastructure for the sample synthesis and gas sensing experiments. We would like to thank the Department of Science and Technology (DST),

Government of India, for awarding the Department of Engineering Physics, K.L.E.F., the DST-FIST Level-1 (SR/FST/PS-1/2018/35) initiative. We want to thank Venkata Satya Chidambara Swamy Vaddadi of N.I.T. Goa for his assistance with the A.F.M. characterisation.

Author contributions

BH contributed to conceptualization, methodology, investigation, data curation, and writing of the original draft, NSMPLD contributed to supervision, methodology, software, formal analysis, and resources, PN contributed to resources and writing,

reviewing, & editing of the manuscript, BRK contributed to conceptualization, supervision, and reviewing & editing of the manuscript.

Funding

No specific grant from any funding agency in the public, private, or not-for-profit sectors was received for this research.

Data Availability

The corresponding author has a copy of the information. Emails might be sent at the reasonable request of the public or a researcher.

Declarations

Conflict of interest The authors certify that none of their known financial conflicts of interest or close personal ties might have influenced the research presented in this study.

References

1. P. Sadhukhan, M. Kundu, S. Rana, R. Kumar, J. Das, P.C. Sil, Microwave induced synthesis of ZnO nanorods and their efficacy as a drug carrier with profound anticancer and antibacterial properties. *Toxicol. Rep.* **6**, 176–185 (2019). <https://doi.org/10.1016/j.toxrep.2019.01.006>
2. C. Yen-Lin, Y. Sheng-Joue, C. Tung-Te, K. Ajit, C. Kuei-Yuan, J. Liang-Wen, Improvement of the UV-sensing performance of Ga-doped ZnO nanostructures via a wet chemical solution at room temperature. *ECS J. Solid State Sci. Technol.* **10**, 127001 (2021). <https://doi.org/10.1149/2162-8777/ac3e43>
3. N.H. Erdogan, T. Kutlu, N. Sedefoglu, H. Kavak, Effect of Na doping on microstructures, optical and electrical properties of ZnO thin films grown by sol-gel method. *J. Alloys Compd.* **881**, 160554 (2021). <https://doi.org/10.1016/j.jallcom.2021.160554>
4. N. X.Li, C.S. ZhangLiu, J. Adimi, D. Zhou, Liu, S. Ruan, Enhanced gas sensing properties for formaldehyde based on ZnO/Zn₂SnO₄ composites from one-step hydrothermal synthesis. *J. Alloys Compd.* **850**, 156606 (2020). <https://doi.org/10.1016/j.jallcom.2020.156606>
5. K. Ravichandran, D.S. Vasanthi, P. Kavitha, R. Shalini, S. Suvathi, P.K. Praseetha, Cost-effective and eco-friendly dye degradation by enzyme-powered ZnO nanomaterial: effect of process temperature. *Bull. Mater. Sci.* **45**, 40 (2022). <https://doi.org/10.1007/s12034-021-02619-8>
6. G.V. Colibaba, D. Rusnac, V. Fedorov, P. Petrenko, E.V. Monaco, Low-temperature sintering of highly conductive ZnO:Ga: Cl ceramics using chemical vapor transport. *J. Eur. Ceram. Soc.* **41**(1), 443–450 (2020). <https://doi.org/10.1016/j.jeurceramsoc.2020.08.002>
7. A. Koo, R. Yoo, S.P. Woo, H.-S. Lee, W. Lee, Enhanced acetone-sensing properties of Pt-decorated Al-doped ZnO nanoparticles. *Sens. Actuators B* **280**, 109–119 (2019). <https://doi.org/10.1016/j.snb.2018.10.049>
8. R. Yoo, T. Andreas, Y. Güntner, H.J. Park, H.-S. Rim, W. Lee, Lee, Sensing of Acetone by Al-doped ZnO. *Sens. Actuators B* **283**, 107–115 (2019). <https://doi.org/10.1016/j.snb.2018.12.001>
9. S.-J. Young, Y.-H. Liu, M.D. Nahin Islam Shiblee, K. Ahmed, L.-T. Lai, L. Nagahara, T. Thundat, T. Yoshida, S. Arya, A. Khosla, *ACS Appl. Electron. Mater.* **2**(11), 3522–3529 (2020). <https://doi.org/10.1021/acsaelm.0c00556>
10. T.H.H. Lynn, A. Jityen, K. Tivakornsasithorn, R. Jaisutti, T. Osotchan, Nano-flower structure of Indium and Gallium doped zinc oxide powder. *Mater. Today: Proc.* **23**(4), 757–761 (2020). <https://doi.org/10.1016/j.matpr.2019.12.270>
11. M. Zahra, A. Ali, A. Khalil, S. Ur Rehman, N. Mushtaq, M. Akbar, R. Raza, Studies of electrical and optical properties of cadmium-doped zinc oxide for energy conversion devices. *Fuel Cells* **21**(2), 164–171 (2021). <https://doi.org/10.1002/fuce.202000026>
12. I. AI.Istrate, C. Mihalache, Romanian et al., Copper doping effect on the properties in ZnO films deposited by sol-gel. *J. Mater. Sci: Mater. Electron.* **32**, 4021–4033 (2021). <https://doi.org/10.1007/s10854-020-05144-2>
13. L. Wang, A. Teleki, S.E. Pratsinis, P.I. Gouma, Ferroelectric WO₃ nanoparticles for acetone selective detection. *Chem. Mater.* **20**, 4794–4796 (2008). <https://doi.org/10.1021/cm800761e>
14. S. Singkammo, A. Wisitorsaat, C. Sriprachubwong, A. Tuantranont, S. Phanichphant, C. Liewhiran, Electrolytically exfoliated graphene-loaded flame-made Ni-Doped SnO₂ Composite Film for Acetone Sensing. *ACS Appl. Mater. Interfaces* **7**, 3077–3092 (2015). <https://doi.org/10.1021/acami.5b00161>
15. Z. Zhang, Z. Wen, Z. Yea, L. Zhu, Gas sensors based on ultrathin porous Co₃O₄ nanosheets to detect acetone at low temperature. *RSC Adv.* **5**, 59976–56285 (2015). <https://doi.org/10.1039/C5RA08536E>
16. M.H. Darvishnejad, A.A. Firooz, J. Beheshtian, A.A. Khodadadi, Highly sensitive and selective ethanol and acetone gas sensors by adding some dopants (Mn, Fe Co, Ni) onto

- hexagonal ZnO plates. RSC Adv. **6**, 7838–7845 (2016). <https://doi.org/10.1039/C5RA24169C>
17. N.H. Al-Hardan, M.J. Abdullah, A.A. Aziz, H. Ahmad, L.Y. Low, ZnO thin films for VOC sensing applications. Vacuum **85**, 101–106 (2010). <https://doi.org/10.1016/j.vacuum.2010.04.009>
 18. S.J. Chang, T.J. Hsueh, I. Chen, S.F. Hsieh, S.P. Chang, C.L. Hsu, Highly sensitive ZnO nanowire acetone vapor Sensor with Au adsorption. IEEE Trans. Nanotechnol. **7**, 754–759 (2008). <https://doi.org/10.1109/TNANO.2008.2005917>
 19. W. Guo, B. Zhao, Q. Zhou, Y. He, Z. Wang, N. Radacsi, N. Fe doped ZnO/reduced graphene oxide nanocomposite with synergic enhanced gas sensing performance for the effective detection of formaldehyde. ACS Omega **4**(6), 10252–10262 (2019). <https://doi.org/10.1021/acsomega.9b00734>
 20. R.K. Malik, R. Khanna, G.L. Sharma et al., Lithium doped zinc oxide thin film hydrogen gas sensor at reduced operating temperature. Sens. Lett. **12**, 1769–1775 (2014). <https://doi.org/10.1166/sl.2014.3402>
 21. L. Utari, N.L.W. Septiani, S. Nugraha, L.O. Nur, H.S. Wasisto, B. Yulianto, Wearable carbon monoxide sensors based on hybrid graphene/ZnO nanocomposites. IEEE Access **8**, 49169–49179 (2020). <https://doi.org/10.1109/ACCESS.2020.2976841>
 22. R. Sankar Ganesh, E. Durgadevi, M. Navaneethan, V.L. Patil, S. Ponnusamy, C. Muthamizhchelvan, S. Kawasaki, P.S. Patil, Y. Hayakawa, Tuning the selectivity of NH₃ gas sensing response using Cu-doped ZnO nanostructures. Sens. Actuator. A: Phys. **269**, 331–341 (2018). <https://doi.org/10.1016/j.sna.2017.11.042>
 23. S. Brahma, P.C. Huang, B.W. Mwakikunga, V. Saasa, A.A. Akande, J.-L. Huang, Chuan-Pu. Liu, Cd doped ZnO nanorods for efficient room temperature NH₃ sensing. Mater. Chem. Phys. (2023). <https://doi.org/10.1016/j.matchemphys.2022.127053>
 24. M. Stankova, X. Vilanova, E. Llobet, J. Calderer, C. Bittencourt, J.J. Pireaux, X. Correig, Influence of the annealing and operating temperatures on the gas-sensing properties of rf sputtered WO₃ thin-film sensors. Sens. Actuators B **105**(2), 271–277 (2005). <https://doi.org/10.1016/j.snb.2004.06.009>
 25. P. Madhukar, N. Jayababu, M.V. Ramana, Reddy, Improved gas sensing performance of Al doped ZnO/CuO nanocomposite-based ammonia gas sensor. Mater. Sci. Engineering: B **227**, 61–67 (2018). <https://doi.org/10.1016/j.mseb.2017.10.012>
 26. V. Shah, J. Bhaliya, G.M. Patel, P. Patel, Joshi, Room-temperature chemiresistive gas sensing of SnO₂ nanowires: a review. J. Inorg. Organomet. Polym. **32**, 741–772 (2022). <https://doi.org/10.1007/s10904-021-02198-5>
 27. F. Pedrotti, M.L. Martins, M. Baloi, C. Magnotti, F. Scheuer, F. Sterzelecki, V. Cerqueira, hematology, and histopathology of common snook *Centropomus undecimalis* (Perciformes: Centropomidae) exposed to acute toxicity of ammonia. J. Appl. Aquac. **30**(3), 272–284 (2018). <https://doi.org/10.1080/10454438.2018.1443049>
 28. P.P. Ricci, O.J. Gregory, Sensors for the detection of ammonia as a potential biomarker for health screening. Sci. Rep. **11**, 7185 (2021). <https://doi.org/10.1038/s41598-021-86686-1>
 29. M.-J. Chan, Y.-J. Li, C.-C. Wu, Y.-C. Lee, H.-W. Zan, H.-F. Meng, M.-H. Hsieh, C.-S. Lai, Y.-C. Tian, Breath ammonia is a useful biomarker predicting kidney function in chronic kidney disease patients. Biomedicine **8**, 468 (2020). <https://doi.org/10.3390/biomedicine8110468>
 30. J.C. Filho, M.Y. Tsuzuki, G. Lemos de Mello, L.C. Miletti, K.H. Lühmann, da Veiga Lima-Rosa, hematology, and histopathology of common snook *Centropomus undecimalis* (Perciformes: Centropomidae) exposed to acute toxicity of ammonia. J. Appl. Aquac. **29**, 3–4 199 (2017). <https://doi.org/10.1080/10454438.2017.1334615>
 31. Y.K. Ip, S.F. Chew, Ammonia production, excretion, toxicity, and defense in fish: a review. Front. Physiol. **1**, 134 (2010). <https://doi.org/10.3389/fphys.2010.00134>
 32. N. Peled, V. Fuchs, E.H. Kestenbaum, E. Oscar, R. Bitran, An update on the use of exhaled breath analysis for the early detection of lung cancer. Lung Cancer **12**, 81–92 (2021). <https://doi.org/10.2147/LCTT.S320493>
 33. T. Chen, T. Liu, T. Li, H. Zhao, Q. Chen, Exhaled breath analysis in disease detection. Clin. Chim. Acta **515**, 61–72 (2020). <https://doi.org/10.1016/j.cca.2020.12.036>
 34. L. Xiang, S. Wu, Q. Hua, C. Bao, H. Liu, A meta-analysis, volatile organic compounds in human exhaled breath to diagnose gastrointestinal cancer: a meta-analysis. Front. Oncol. **11**, 269 (2021). <https://doi.org/10.3389/fonc.2021.606915>
 35. F. Mouzaia, D. Djouadi, A. Chelouche, L. Hammiche, T. Touam, Particularities of pure and Al-doped ZnO nanostructures aerogels elaborated in supercritical isopropanol. Arab J. Basic Appl. Sci. **27**(1), 423–430 (2020)
 36. P. Scherrer, Bestimmung der Grösse und der inneren Struktur von Kolloidteilchen mittels Röntgenstrahlen. Nachr. Ges Wiss Göttingen **26**, 98 (1918)
 37. J.I. Langford, A.J.C. Wilson, Scherrer after sixty years: a survey and some new results in the determination of Crystallite size. J. Appl. Cryst. **11**, 102 (1978)
 38. M. Ahmad, E. Ahmed, Y. Zhang, N.R. Khalid, J. Xu, M. Ullah, Z. Hong, Preparation of highly efficient Al-doped ZnO photocatalyst by combustion synthesis. Curr. Appl. Phys. **13**(4), 697–704 (2013). <https://doi.org/10.1016/j.cap.2012.11.008>

39. C. Belkhaoui, N. Mzabi, H. Smaoui, P. Daniel, Enhancing the structural, optical, and electrical properties of ZnO nanopowders through (Al + Mn) doping. *Results Phys.* **12**, 1686–1696 (2019). <https://doi.org/10.1016/j.rinp.2019.01.085>
40. J. Wojnarowicz, T. Chudoba, W. Lojkowski, A review of microwave synthesis of Zinc Oxide Nanomaterials: reactants, process parameters, and Morphologies. *Nanomaterials* **10**(6), 1086 (2020). <https://doi.org/10.3390/nano10061086>
41. Y.-H. Zhang, Y.-L. Li, F.-L. Gong, K.-F. Xie, M. Liu, H.-L. Zhang, S.-M. Fang, Al doped narcissus-like ZnO for enhanced NO₂ sensing performance: an experimental and DFT investigation. *Sens. Actuators B* **305**, 127489 (2019). <https://doi.org/10.1016/j.snb.2019.127489>
42. A. Abdelkhalik, A.A. Al-Askar, Green synthesized ZnO nanoparticles mediated by *Mentha Spicata* extract induce plant systemic resistance against *Tobacco Mosaic Virus*. *Appl. Sci.* **10**(15), 5054 (2020). <https://doi.org/10.3390/app10155054>
43. S.S. Rad, A.M. Sani, Mohseni, characterization and antimicrobial activities of zinc oxide nanoparticles from leaf extract of *Mentha pulegium* (L.) *Microb. Pathog* **131**, 239–245 (2019). <https://doi.org/10.1016/j.micpath.2019.04.022>
44. R. Mohammadi-Aloucheh, A. Habibi-Yangjeh, A. Bayrami, S. Latifi-Navid, A.J. Asadi, Green synthesis of ZnO and ZnO/CuO nanocomposites in *Mentha longifolia* leaf extract: characterization and their application as antibacterial agents. *Mater. Sci. Mater. Electron.* **29**, 13596–13605 (2018). <https://doi.org/10.1007/s10854-018-9487-0>
45. S.-S. Lo et al., Raman scattering and bandgap variations of Al-doped ZnO nanoparticles synthesized by a chemical colloid process. *J. Phys. D Appl. Phys.* **42**, 095420 (2009). <https://doi.org/10.1088/0022-3727/42/9/095420>
46. H. Viola, S. Eva, S. Nadezda, Characterization of cellulosic fibers by FTIR spectroscopy for their further implementation to building materials. *Am. J. Anal. Chem.* (2018). <https://doi.org/10.4236/ajac.2018.96023>
47. K.J.R. N.Srinatha, M.R.S. Kumar, Kumar, Combustion synthesis of Al-doped ZnO nanoparticles using a new fuel and the study of its structural, microstructural, and optical properties. *Appl. Nanosci.* **11**(4), 1197–1209 (2021). <https://doi.org/10.1007/s13204-021-01689-8>
48. S. Singhal, J. Kaur, T. Namgyal, R.Sharma, Cu-doped ZnO nanoparticles: synthesis, structural and electrical properties. *Phys. B: Condens. Matter.* **407**, 1223–1226 (2012). <https://doi.org/10.1016/j.physb.2012.01.103>
49. Y. Wang, M. Yu, C. Huang, Q. Zheng, H. Zhou, Z. Zhang, S. Zhao, Infrared emission characteristic and microwave loss property of aluminium-doped zinc oxide nanoparticles. *Ceram. Int.* **47**(2), 2456–2462 (2021). <https://doi.org/10.1016/j.ceramint.2020.09.088>
50. G. Kaur, A. Mitra, K.L. Yadav, Pulsed laser deposited Al-doped ZnO thin films for optical applications. *Prog. Nat. Sci.: Mater. Int.* **25**(1), 12–21 (2015). <https://doi.org/10.1016/j.pnsc.2015.01.012>
51. F. Ajala, A. Hamrouni, A. Houas, H. Lachheb, B. Megna, L. Palmisano, F. Parrino, The influence of Al doping on the photocatalytic activity of nanostructured ZnO: the role of adsorbed water. *Appl. Surf. Sci.* **445**, 376–382 (2018). <https://doi.org/10.1016/j.apsusc.2018.03.141>
52. H. Rasheed, A. Kareem, Effect of multiwalled carbon nanotube reinforcement on the opto-electronic properties of polyaniline/c-Si heterojunction. *J. Opt. Commun.* **42**(1), 25–29 (2021). <https://doi.org/10.1515/joc-2018-0024>
53. H.A. Varudkar, G. Umadevi, P. Nagaraju, Fabrication of Al-doped ZnO nanoparticles and their application as a semiconductor-based gas sensor for the detection of ammonia. *J. Mater. Sci: Mater. Electron.* **31**, 12579–12585 (2020). <https://doi.org/10.1007/s10854-020-03808-7>
54. R. Kant, V. Chanchal, Enhancement in dielectric and optical properties of Al doped ZnO/ reduced graphene oxide nanocomposite. *Mater. Technol.* **37**, 8 655–662 (2022). <https://doi.org/10.1080/10667857.2020.1868745>
55. Y. Caglar et al., Microstructural, optical and electrical studies on sol gel derived ZnO and ZnO: Al films. *Curr. Appl. Phys.* **12**(3), 963–968 (2012). <https://doi.org/10.1016/j.cap.2011.12.017>
56. I. Al-Ajaj, A. Kareem, Synthesis and characterization of polyimide thin films obtained by thermal evaporation and solid state reaction. *Mater. Sci.-Poland* **34**(1), 132–136 (2016). <https://doi.org/10.1515/msp-2016-0029>
57. S. Hosseinabadi, F. Abrinaei, M. Shirazi, Statistical and fractal features of nanocrystalline AZO thin films. *Phys. Stat. Mech. Appl.* **481**, 11–22 (2017). <https://doi.org/10.1016/j.physa.2017.03.033>
58. P.R. Kalvani, A. Jahangiri, S. Shapouri, A. Sari, Y.S. Jalili, Multimode AFM analysis of aluminum-doped zinc oxide thin films sputtered under various substrate temperatures for optoelectronic applications. *Superlattices Microstruct.* **132**, 106173 (2019). <https://doi.org/10.1016/j.spmi.2019.106173>
59. Y. Vijayakumar, P. Nagaraju, V. Yaragani, S.R. Parne, N.S. Awwad, Nanostructured Al and Fe co-doped ZnO thin films for enhanced ammonia detection. *Phys. B: Condens. Matter.* **581**, 411976 (2020). <https://doi.org/10.1016/j.physb.2019.411976>
60. F. Ambroz, T.J. Macdonald, V. Martis, V.P. Parkin, Evaluation of the BET theory for the characterization of Meso and Microporous MOFs. *Small Methods* **2**, 1800173 (2018). <https://doi.org/10.1002/smt.201800173>
61. A.N. A.Anasthasiya, S. Ramya, D. Balamurugan et al., Adsorption property of volatile molecules on ZnO nanowires:

- computational and experimental approach. *Bull. Mater. Sci.* **41**, 4 (2018). <https://doi.org/10.1007/s12034-017-1538-2>
62. K.S.W. Sing, D.H. Everett, R.A.W. Haul, L. Moscou, R.A. Pierotti, J. Rouquerol, T. Siemieniowska, Reporting physisorption data for gas/solid systems with special reference to the determination of surface area and porosity. *Pure Appl. Chem.* **57**, 603–619 (1985). <https://doi.org/10.1351/pac198557040603>
63. B. Zdravkov, J. Čermák, M. Šefara, Pore classification in the characterization of porous materials: a perspective. *Open Chem.* **5**(2), 385–395 (2007). <https://doi.org/10.2478/s11532-007-0017-9>
64. J. Mohanraj, D. Durgalakshmi, R. Ajay, Rakkesh, Selective room temperature ammonia gas sensor using nanostructured ZnO/CuO@graphene on a paper substrate. *Sens. Actuators: B Chem.* **350**, 130833 (2022). <https://doi.org/10.1016/j.snb.2021.130833>
65. G. Alexieva, K. Lovchinov, M. Petrov, R. Gergova, N. Tyutyundzhiev, Influence of Al doping on the morphological structural and gas sensing properties of electrochemically deposited ZnO films on quartz resonators. *Coatings* **12**(1), 81 (2022). <https://doi.org/10.3390/coatings12010081>
66. F. Shu Xing, T. Wei, Synthesis, characterization, and mechanism of electrospun carbon nanofibers decorated with ZnO nanoparticles for flexible ammonia gas sensors at room temperature. *Sens. Actuators: B Chem.* **362**, 131789 (2022). <https://doi.org/10.1016/j.snb.2022.131789>
67. K.R. Devi, G. Selvan, M. Karunakaran, Enhanced room temperature ammonia gas sensing properties of Al-doped ZnO nanostructured thin films. *Opt. Quant. Electron.* **52**, 501 (2020). <https://doi.org/10.1007/s11082-020-02621-0>
68. L.H. Kathwate, G. Umadevi, P.M. Kulal, P. Nagaraju, D.P. Duba, A.K. Nanjundan, V.D. Mote, *Sens. Actuators A: Phys.* **313**, 112193 (2020). <https://doi.org/10.1016/j.sna.2020.112193>
69. A. Jagan Mohan Reddy, N.K. Katari, P. Nagaraju, S.M. Surya, ZIF-8, Zn(NA) and Zn(INA) MOFs as chemical selective sensors of ammonia, formaldehyde and ethanol gases. *Mater. Chem. Phys.* (2020). <https://doi.org/10.1016/j.matchemphys.2019.122357>
70. P.S. Kolhe, A.B. Shinde, S.G. Kulkarni, N. Maiti, P.M. Koinkar, K.M. Sonawane, The gas-sensing performance of Al doped ZnO thin film for H₂ S detection. *J. Alloys Compd.* **748**, 6–11 (2018). <https://doi.org/10.1016/j.jallcom.2018.03.123>
71. A. Handan, Y. Fahrettin, A. Cihat, Al-doped ZnO as a multifunctional nanomaterial: structural, morphological, optical and low-temperature gas sensing properties. *J. Alloys Compd.* **773**, 802–811 (2019). <https://doi.org/10.1016/j.jallcom.2018.09.327>

Publisher's Note Springer Nature remains neutral with regard to jurisdictional claims in published maps and institutional affiliations.

Springer Nature or its licensor (e.g. a society or other partner) holds exclusive rights to this article under a publishing agreement with the author(s) or other rightsholder(s); author self-archiving of the accepted manuscript version of this article is solely governed by the terms of such publishing agreement and applicable law.